Photothermal MXenes-embedded tannin-Eu^{3+} particles constructed for accelerating infected seawater immersion wound healing and persistent anti-infection by forming in situ bacterial vaccines

Zhentao Li [a,1], Ting Song [b,1], Yanpeng Jiao [a], Zijing Zhu [c], Yang Liao [c,*], Zonghua Liu [b,*]

[a] Department of Materials Science and Engineering, Jinan University, Guangzhou 510632, China

[b] Department of Biomedical Engineering, Jinan University, Guangzhou 510632, China

[c] Department of Laboratory Medicine, General Hospital of Southern Theatre Command of PLA, Guangzhou 510010, China

*Corresponding authors:

Zonghua Liu (tliuzonghua@jnu.edu.cn)

Yang Liao (liaoyangswh@163.com)

[1] These authors contributed equally to this work and should be considered as co-first authors.

Abstract

The low temperature, high salt content and bacteria in the seawater environment can induce severe infections of open wounds, making them difficult to heal. To date, numberous wound dressings have been developed with functions in repairing injuries and various anti-bacterial functions. However, ordinary anti-bacterial strategies could not provide long-lasting resistance to infection to promote wound healing. Here, we reported a strategy to build a durable resistance to seawater immersion wound infection by killing bacteria and delivering bacterial antigens in situ. Specifically, MXenes-embedded tannin-Eu^{3+} particles (M@TA-Eu) were constructed to effectively repair the infected seawater immersion injuries and fight infection in a lasting manner by forming in situ bacterial vaccines and immune memory. In the particle, the platform constructed by TA and Eu^{3+} had pro-vascularization and antigen presentation effects. The MXenes with near-infrared photothermal effect were introduced to kill the bacteria and promote the recruitment of antigen presentation cells to enhance vaccination efficacy. The experimental results showed that the particles not only effectively improved the healing of injuries by relieving wound inflammation and inhibiting bacteria, but also produced potent vaccination effect by forming *in situ* bacterial vaccines. Therefore, the M@TA-Eu particles provided novel strategy for the development of high-grade dressings for anti-infection.

Key words: MXenes; Tannin; Wound healing; Anti-infection; In situ vaccines

1 Introduction

The treatment need of seawater immersion wounds is growing along with more ocean research and marine military activities [1, 2]. Compared with ordinary wounds, seawater immersion wounds are more complex and difficult to heal. Firstly, the hypothermic seawater lowers the temperature of injured tissues and reduces the immunity of body, increasing the risk of wound infection. Secondly, hypersaline hypertonic seawater aggravates the damage and energy consumption of injured tissues by increasing the osmotic pressure, and leads to the necrosis of peripheral vascular tissues and the excess free radical accumulation [3]. In addition, the potential risk of wound infection from the presence of pathogenic bacteria in seawater is not negligible. The alkaline seawater immersion leads to an increase in injured tissue pH, which not only hinders the proliferative activity of injured tissue but also facilitates the proliferation of bacteria on the injured tissue surface [4]. The harsh environment of the seawater increases the risk of wound infection and predisposed to chronic refractory wounds and life-threatening complications [5]. Severe infection of the wound is a major obstacle to its healing. At present, as a necessary intervention in the management of injured treatment, the performance of current dressings can not establish a robust and long-lasting anti-infection mechanism for the complicated and refractory infected seawater immersion wounds. For the characteristics of infected seawater immersion wounds, the ideal functional dressing should have the ability to scavenge excess reactive oxygen species (ROS). In particular, it should establish a durable anti-infection mechanism to promote healing.

The bacterial infection is usually a serious problem in wound treatment, which could even cause systemic lethal infection. Establishing a durable anti-infection mechanism is an effective way to deal with refractory wound infection. However, the uncontrollable release of antimicrobial agents from drug-carrying dressings makes long-acting anti-infection strategy ineffective. Also, the well-known

resistance of the bacteria to antibiotics often causes anti-infection failure. To avoid the shortcomings of antibiotics, novel methods have been developed, such as photo-thermal and photodynamic anti-bacterial therapies [6, 7]. The photo-thermal therapy triggered by near-infrared light (NIR) is a promising sterilization strategy with a combination of minimal invasiveness, low toxicity and few side effects [8, 9]. However, the killing ability of photothermal treatment on bacteria in deep wound is still limited. To solve the infection problem once and for all often relies on the use of vaccines, which can automatically fight specific pathogens in each infection event by producing lasting immune memory. Even so, conventional vaccination has not become a universal anti-infection strategy, due to the limited vaccine categories and amount, the complicated and expensive vaccine development and production process, and frequent antigenic mutations. In recent years, newly emerging in situ vaccine strategy provides novel sight to solve the wound infection problem once and for all. In anti-tumor studies, in situ tumor vaccines have been widely constructed to overcome the low immunogenicity and frequent antigenic mutations of tumor cells [10, 11]. Also, in situ vaccination strategy was adopted to treat bacterial osteomyelitis by immunotherapy [12]. In particular, Prof. Jeremiah J. Gassensmith constructed an in situ bacterial vaccine by metal−organic framework to improve bacteremia survival [13]. From the above information, the in situ vaccination seems to be a promising strategy to optimally solve the durable resistance to infection and repeated wound infection problems. Interestingly, related studies have shown that the photothermal response exhibits an enhanced effect on immunotherapy, mainly by inducing immunogenic cell death and enhancing immunotherapy through the release of damage-associated molecular patterns [14-17]. Therefore, we envision the construction of an in situ bacterial vaccine that is composed of a photothermal response process and in situ bacteria at the wound. And it can stimulate the body's immune system in real time for the establishment of a long-lasting anti-

infection mechanism.

For better stimulation of immune cells, an effective mediator of antigen presentation or vaccine adjuvants is required. As a natural polyphenolic material, tannin (TA) exhibits good antioxidant properties and biocompatibility, which has been shown to be effective in scavenging harmful free radicals from wounds to reduce oxidative stress [18]. Particularly, relevant experiments have confirmed that TA can be used as a novel candidate for vaccine molecular-structure adjuvant [19, 20]. Also, the rich phenolic hydroxyl groups of TA provide effective binding sites to functional metal ions. Some functional metal ions have been reported to have effective pro-repair effects [21]. Therefore, based on the coordination of TA and Eu^{3+}, it is expected that a functional adjuvant particle with antioxidant pro-vascularizing and antigen-presenting properties will be constructed.

Here, a multifunctional MXenes-embedded tannin-Eu^{3+} composite particles (M@TA-Eu) was constructed to effectively repair the infected seawater immersion wounds and persistently fight infection by forming in situ bacterial vaccines. The tannin-Eu^{3+} frame not only provide an effective platform for effective contact with wound bacteria and antigen presentation, but also exhibit antioxidant capabilities to promote rapid wound healing. The MXenes with NIR photothermal effect can effectively kill bacteria and synergize with TA to promote the in situ vaccination efficacy [22]. The killed bacteria form in situ vaccines, which is presented by the particles to induce strong vaccine efficacy against reinfection once and for all. These properties of the M@TA-Eu particles were investigated *in vitro* and *in vivo*.

2 Materials and Methods

2.1 Materials

TA, $Eu(NO_3)_3 \cdot 6H_2O$ (99.99%), NaOH, and 2′,7′-dichlorodihydrofluorescein diacetate (H_2DCFDA) were purchased from Aladdin Reagent (Shanghai China). Ti_3AlC_2, HF, H_2O_2, and tetrapropylammonium hydroxide (TPAOH) were obtained from Guangzhou Chemical Reagent Plant (Guangzhou, China). The bacterial strains including *E.coli ATCC25922* and *S. aureus ATCC 29213* were acquired from Guangzhou Scissorhands Gene Technology Co., Ltd.(Guangzhou, China). The agar and lysogeny broth were obtained from Shanghai McLean Biochemical Technology Co., Ltd (Shanghai, China). The lipopolysaccharides originating from *E. coli* and *Pseudomonas aeruginosa* were procured from Beijng Biosynthesis Biotechnology Co., Ltd and Sigma-Aldrich, respectively. The SPA recombinant *Staphylococcus aureus* protein A was obtained from Solarbio Science & Technology Co., Ltd. (Beijing, China). The (Cell Counting Kit-8) CCK-8 and the (Acridine Orange/Ethidium Bromide) AO/EB fluorescent staining kits were purchased from Solarbio Science & Technology Co., Ltd. (Beijing, China). Dulbecco's modified Eagle's medium (DMEM), fetal bovine serum (FBS), DAPI and phosphate buffered saline (PBS) were bought from Thermo Fisher Scientific (China) Co., Ltd. All animal experiments in this study were approved by the Animal Ethics Committee of Jinan University and carried out in accordance with the relevant regulations (the assigned approval/accreditation number: SYXK(Guangdong) 2022-0174).

2.2 Preparation of Ti_3C_2 MXenes

Briefly, Ti_3AlC_2 powders (5 g) were etched for 72 h in HF solution (100 mL, 40% wt%) at room temperature. Then, the treated powders were collected by centrifugation (15000 rpm, 10 min) and washed with deionized water and ethanol for several times. Next, TPAOH solution (100 mL, 25% wt%) was used to further oxidize the HF- etched Ti_3C_2 nanosheets for 72 h at room temperature. The oxidized Ti_3C_2 nanosheets were collected by centrifugation (15000 rpm, 10 min) and washed with deionized

water and ethanol for several times. Finally, the formed Ti_3C_2 MXenes were obtained after lyophilization.

2.3 Preparation of the M@TA-Eu particles

The M@TA-Eu particles were prepared by a simple and mild reaction. The obtained MXenes powders were added into TA solution (20 mg/mL in deionized water) to form 1 mg/mL MXenes suspension, which was stirred for 30 min. Then, the suspension was treated with ultrasonic (100 W) for 24 h at 0ºC. After standing for 10 min, the supernatant was collected. The same volume of $Eu(NO_3)_3$ solution (5 mg/mL in deionized water) was added dropwise to the supernatant under vigorous stirring. Next, NaOH solution (1 M) was slowly added dropwise under ultrasonication treatment (100 W) to regulate the pH of the mixture to 8.5. After stirring for 24 h at room temperature, the formed M@TA-Eu particles were collected by centrifugation (10000 rpm, 10 min). The obtained particles were further washed with deionized water to regulate the pH to 7~7.5. Finally, the M@TA-Eu particles were obtained by freeze-drying (Figure 1). According to the final concentration of the MXenes, the particles were labeled as TA-Eu, $M_{0.5}$@TA-Eu, M_1@TA-Eu, and M_2@TA-Eu, respectively.

2.4 Physical and chemical properties of the M@TA-Eu particles

The morphology of particles was obtained by a scanning electron microscope (SEM, XL30 FESEM FEG, PHILIPS) with an accelerating voltage was 5 kV. The mapping of Eu^{3+} and Ti^{3+} in M@TA-Eu particles was observed by an X-ray energy-dispersive spectroscopic (EDS) detector attached to SEM. The other characterization methods including Fourier transformation infrared (FTIR, Bruker EQUINOX 55 FTIR, Germany), Raman spectra (FT Bruker RFS 106/S, America), X-ray diffraction (XRD, MiniFlex-600, Rigaku Corporation, Japan), and thermogravimetric analysis (TGA, 209F3-ASC, Netzsch, Germany) were available in Supporting Information Materials and Methods. The release

behaviors of TA and Eu^{3+} from the particles were evaluated. In general, the particles (2 mg) were incubated in PBS (pH5.0 or pH7.4, 4 mL) for 72 h. The entire sustained-release system was performed on a thermostatic shaker (37ºC) to simulate the slow-release effect at the infected wound site. At a specific time, the incubated PBS solution was collected by centrifugation and supplemented with an equal amount of fresh PBS solution. Finally, the UV spectroscopy was used to evaluated the absorbances of TA at 280 nm. The TA concentration released from particles was detected based on the standard curve. In addition, inductively coupled plasma-optical emission spectroscopy (ICP-OES) was employed to evaluated the cumulative release concentration of Eu^{3+}.

2.5 Photothermal effect of the M@TA-Eu particles

The particles solutions with a concentration of 250 μg/mL were prepared to investigate the photothermal efficiency. A laser beam (808 nm, 2 W/cm^2) was employed to irradiate these particles solutions for 10 min. In the process, the temperature of the solutions was recorded at 30 s intervals using digital thermometer (TES1310) and the infrared photos was obtained by a thermal imager at 2 min intervals. Also, the photothermal response of the particles under natural sunlight was evaluated.

2.6 The antioxidant activity of the M@TA-Eu particles

The evaluation of the ROS scavenging capacity of the particles referred to the method we previously reported [23]. Briefly, the ability of the particles to scavenge DPPH (1,1-diphenyl-2-picryl hydrazyl) free radical at 517 nm was recorded by UV-vis [24]. The hydrogen peroxide assay kit and the SOD assay kit were employed to assess the catalase activity and the superoxide anion scavenging activity of the particles. Also, the scavenging effect of the particles on L929 cellular ROS was evaluated [25]. The details were available in Supporting Information Materials and Methods.

2.7 Cell viability

The proliferation and viability of human umbilical vein endothelial cells (HUVECs) and mouse fibroblasts (L929) incubated with the particles were assessed by the CCK-8 kit and AO/EB fluorescent staining.

2.8 The antibacterial activity of the M@TA-Eu particles

The *Escherichia coli* (*E. coli*) and *Staphylococcus aureus* (*S. aureus*) strains were employed to evaluate the antibacterial activity of the particles according to the growth status and survival ratio of bacterial. Briefly, the bacterial strains (~10^8 CFU/mL, 100 μL) were incubated with sterile particles (250 μg/mL) with shaking (150 rpm) at 37ºC for 24 h. Also, the same culture system with 10 min of a laser beam (808 nm, 2 W/cm^2) irradiation was assessed. These incubated bacterial broth (100 μL) were diluted 1x10^4 times using sterile pH7.4 PBS, and then a small amount of diluent (100 μL) was inoculated in sterile solid agar medium for further cultivation for 24 h in a carbon dioxide incubator (37ºC, 5% CO_2). Finally, the growth status and the survival rate of bacteria were evaluated.

The morphological changes of the bacteria before and after cultivation were observed. The incubated bacteria were collected by centrifugation and then washed with pH7.4 PBS for 3 times. Next, the morphology of bacterial cells was fixed with paraformaldehyde (4%) for 12 h at 4ºC. Afterwards, the bacteria were washed with pH7.4 PBS for 3 times and dehydrated with a series of ethanol (30, 50, 70, 80, 90, 95, and 100%). At last, the morphology of bacteria was observed by the SEM.

2.9 In vivo wound healing

Healthy adult male Sprague Dawley rats (250-300 g) were divided into five groups (3 rats in each group). Four standardized full-thickness skin wounds (diameter: 10 mm) were established on both sides of each rat's back. Then, these wounds were exposed for 1 h to 17-20ºC simulated seawater, and then to the 0.1 mL suspension containing *S. aureus, E. coli, and P. aeruginosa* (each: ~10^8 CFU/mL).

These wounds were treated with sterile gauze, TA-Eu, M_2@TA-Eu, and M_2@TA-Eu+NIR, respectively. The NIR irradiation was conducted daily for 15 min at 2 W/cm^2 for 3 days. All the wounds were dressed with 3M micropore surgical adhesive tapes to isolate airborne bacteria and prevent the dressing from falling off. The dressings were changed every three days. On day 3, 7 and 11, the healing of wounds was recorded. Moreover, the uninfected acute injury (no seawater immersion) wrapped in sterile gauze was used as a control to assess the repair effect. The wound healing ratio was calculated by the following formula:

$$\text{Wound healing rate (\%)} = \frac{A_0 - A_t}{A_0} \times 100\%$$

in which, the A_0 and A_t evaluated by ImageJ software were the initial wound area on day 0 and day t, respectively.

The structure and collagen deposition in newly formed skin were evaluated by Hematoxylin and Eosin (H&E)-stained, and Masson's trichrome. The stained histological sections information (5 μm thickness) was recorded by an optical microscope (DMI3000B, Leica). Also, after the sections were blocked with 5% serum, the immunohistochemical staining was evaluated, including IL-1β, IL-6, TGF-β1, CD31 and α-SMA, respectively.

2.10 Determination of colony forming unit counts

On day 3 after the surgery, the colonization of wound bacteria was counted. Briefly, the excised skin tissue was homogenized in sterile saline (3 mL). Serially diluted tissue homogenates (100 μL) using sterile saline were evenly spread on agar medium. In the process, mannitol salt agar, VRBA-MUG, and *P. aeruginosa* selection media were employed to selectively culture *S. aureus, E. coli, and Pseudomonas aeruginosa*, respectively. The growth of the colonies was recorded by taking photos,

and the number of the corresponding bacteria on the wounds was counted.

2.11 In situ vaccination efficacy analysis

To evaluate the efficacy of the formed in situ bacterial vaccines, key vaccination evaluations were performed. Briefly, 45 healthy adult male Sprague Dawley rats (150-200 g) were divided to three groups (15 rats in each group). Standardized full-thickness skin wounds (diameter: 10 mm) were established on the rats' back. Then, these wounds were exposed for 1 h to 17-20ºC simulated seawater, and then to the 0.1 mL suspension containing *S. aureus, E. coli, and P. aeruginosa* (each: ~10^8 CFU/mL). The infected wounds were treated with sterile gauze as a negative control, M_2@TA-Eu, and M_2@TA-Eu+NIR, respectively. The NIR light irradiation was carried out daily for 15 min at 2 W/cm^2 for 3 days. All the wounds were dressed with 3 M micropore surgical adhesive tapes to isolate airborne bacteria and prevent the dressing from falling off. The dressings were changed every three days.

After 2 days of the wound treatment with the dressings, five rats from each group were randomly sampled to evaluate the key biological indexes of dendritic cells (DCs). First, the spleens of the rats were collected after their euthanasia, and grinded to splenocytes. Then, the splenocytes (1×10^6 cells/rat) were stained with fluorescently-labeled antibodies (anti-CD11c-APC, anti-MHC I-PE, anti-MHC II-PE, anti-CD80-FITC, and anti-CD86-PerCP-Cy5.5). After re-suspended with PBS, the cells were measured with a flow cytometer (Beckman Coulter, USA) to detected the expression percentages of MHC I, MHC II, CD40, CD80and CD86 molecules on $CD11c^+$ DCs. The data were analyzed with the attached CytoExpert software.

After 7 days of the wound treatment with the dressings, five rats from each group were randomly sampled to evaluate the key biological index of DCs, the bacteria-specific antibody IgG titers and key cytokines levels produced in the rats. First, the blood samples of the rats were collected for the

preparation of their sera. Then, the spleens of the rats were collected after their euthanasia, and grinded to splenocytes. Then, the splenocytes (5×10^6 cells/mL, 2 mL) of each group were planted into 12-well plates, and re-stimulated with representative antigens of the three bacteria at the final concentration of 25 μg/mL. After 60 h of incubation in a cell incubator at 37ºC with 5% CO_2, the cell supernatants were collected for the detection of the cytokines secretion levels. Among them, the key biological indexes of DCs were evaluated with the same protocols as mentioned above. The bacteria-specific antibody IgG titers produced in the rats were measured with an enzyme linked immunosorbent assay (ELISA). The key cytokines levels produced in the rats were measured with an ELISA kit.

After 40 days of the wound treatment with the dressings, five rats left in each group were sampled to re-evaluate the bacteria-specific antibody IgG titers produced in the rats by using the same protocols as mentioned above.

2.12 Statistical analysis

All results were expressed as the mean ± SD (standard deviation). SPSS was employed to assess the significance of differences between data, and the significance level was expressed as *$p < 0.05$, **$p < 0.01$, and ***$p < 0.001$.

3 Results and discussion

3.1 Preparation and characterization of the M@TA-Eu particles

The good dispersion of MXenes was a prerequisite for M@TA-Eu particles with fast photothermal response. In this work, the obtained MXenes exhibited a loose laminar structure (Figure S1a), and displayed a size of about 600 nm after ultrasonic treatment (Figure S1b). The layer thickness of the MXenes was about 1-1.5 nm, indicating that MXenes were dispersed in a monolayer/few-layer state (Figure S1c) [26].

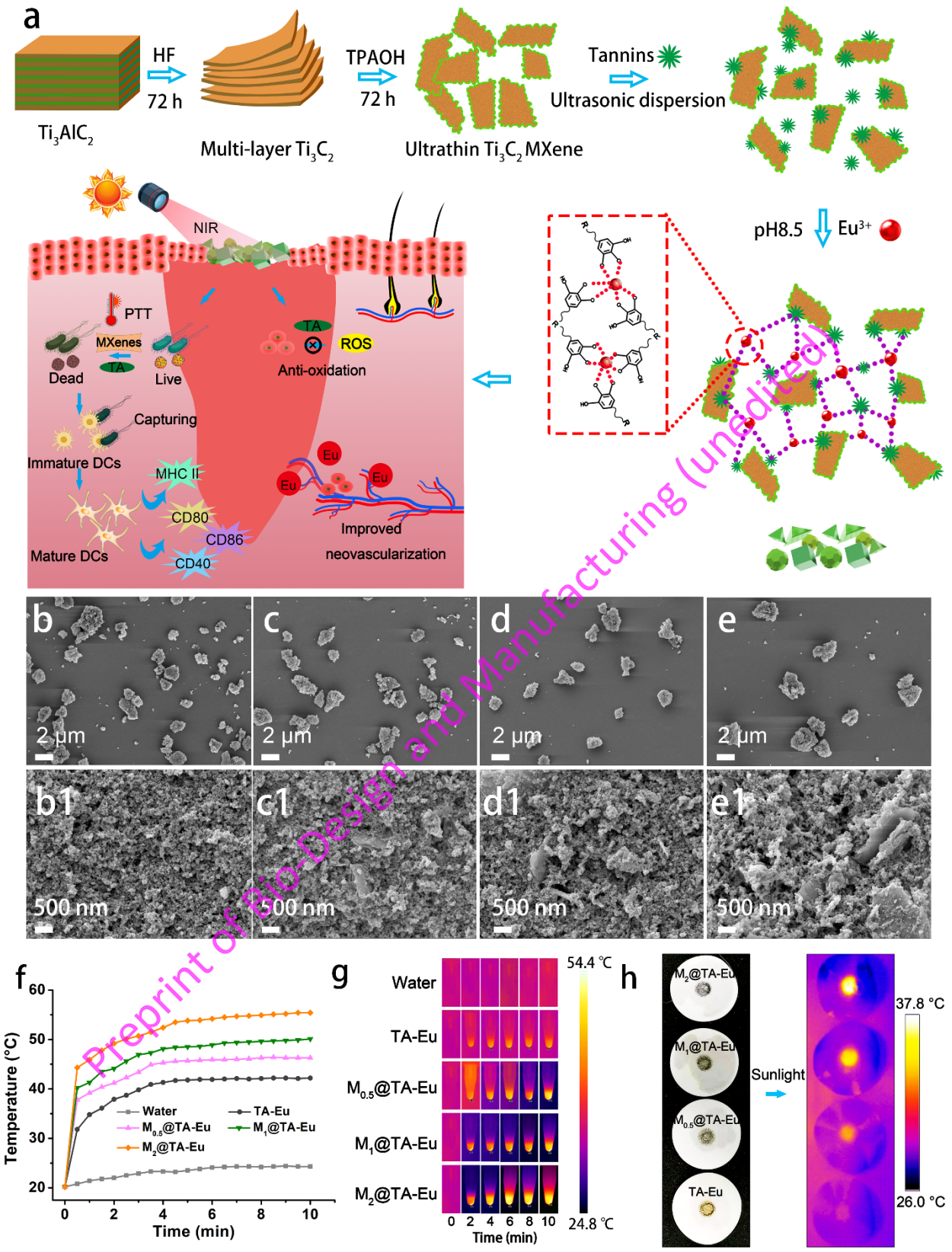

Figure 1 Fabrication of M@TA-Eu complexes (a); SEM images of M@TA-Eu complexes: TA-Eu (b, b1), $M_{0.5}$@TA-Eu (c, c1), M_1@TA-Eu (d, d1), and M_2@TA-Eu (e, e1); Temperature variation of the M@TA-Eu complexes solutions

with a concentration of 250 μg/mL under NIR light irradiation (808 nm, 2 W/cm^2) (f); Infrared thermography of the M@TA-Eu complexes (250 μg/mL) under NIR light irradiation (808 nm, 2 W/cm^2) (g) and sunlight (h).

The preparation of the particles was mainly constructed based on the coordination interaction between TA and Eu^{3+} in an alkaline environment (pH=8.5), in which the weak interaction between TA and MXenes and the adsorption of MXenes on Eu^{3+} allowed MXenes to be embedded in the particles (Figure 1a). The morphology of the M@TA-Eu particles was observed by using SEM. The particles have a size range of about 2 μm (Figure 1b-e) and exhibited a microporous structure (Figure 1b1-e1). In addition, the effective embedding of MXenes was clearly observed in all the M@TA-Eu particles. Also, the EDS mapping of Ti and Eu elements indicated the uniform structure of the particles (Figure S2). These tiny particles are more likely to diffuse into the deeper tissues and make full contact with deep bacteria inside the wound.

The weakening of the TA infrared characteristic peaks (Figure S3a) confirms the coordination interaction between TA and Eu^{3+}, i.e. C=O vibration (~1716 cm^{-1}), C=C stretching vibration of the benzene rings (~1616 cm^{-1}), C-O stretching vibration of the carboxyl group (~1323 cm^{-1}), and C-OH vibration of the benzene rings (~1188 cm^{-1}) [27, 28]. The MXenes did not cause significant changes in the FITR spectrum of the TA-Eu particles. The XRD analysis showed that the crystalline structure of the TA-Eu particles changed with the MXenes embedding. Mainly, the XRD diffraction peaks of the MXenes become more pronounced, such as the (002) and (110) peaks shown at 2θ=6.7° and 61° (Figure S3b) [29, 30]. Also, four typical Raman bands located at ~148, 266, 405, and 604 cm^{-1}, which were ascribed to ω1, ω2, ω3, and ω4 Raman-active phonon vibration modes of the MXenes (Figure S3c) [31]. The benzene structure in TA exhibited characteristic D (~1363 cm^{-1}) and G (1577 cm^{-1})

peaks [32]. In addition, the embedding of MXenes improved the thermal stability of the particles (Figure S3d), which may be caused by the inherent high thermal stability of MXenes [33]. During the heating process, MXenes changed in weight loss and weight gain, which were based on the removal of oxygen-containing functional groups and the formation of oxides caused by the introduction of oxygen atoms, respectively. And the final residual rate of MXenes remained at 92.89%. The thermal dissociation of TA occurs at~ 200°C. Based on the TA and Eu^{3+} coordination interactions, the thermal dissociation of TA-Eu occurs at ~250°C. Subsequently, the breaking of the chemical bond between TA and Eu and the formation of metal oxides occurred at ~300°C. The introduction of MXenes raised the dissociation temperature of particles, including the thermal stability of TA and TA-Eu chemical bonds. Finally, the increase in the residual rate of the particles corroborated the effective introduction of MXenes.

3.2 Photothermal effect of the M@TA-Eu particles

As reported, MXenes have a high extinction coefficient (25.2 L/g•cm, 808 nm), a high photothermal conversion efficiency (~ 30.6%), and a local plasmon resonance effect (LSPR), which allows them to exhibit a better photothermal conversion efficiency than other materials, such as graphene, gold nanorods, black phosphorus quantum dots, CuS_2, and MoS_2 [34-38]. In this work, the introduction of MXenes allows the particles to have a more sensitive photothermal response for the effectiveness of interventions on seawater immersion infected wound. As shown in Figure 1f, the non-radiative transition of some electrons in the TA-Eu particles under NIR irradiation was responsible for their photothermal response behavior, which showed a moderate temperature change. By contrast, the M@TA-Eu particles had a more pronounced heating effect under NIR irradiation, which can achieve a rapid temperature rise within 30 s. Also, the heating effect was observed in the infrared thermograms

(Figure 1g). Moreover, the M_2@TA-Eu particles exhibited good photothermal stability based on the stable coordination interaction of TA and Eu^{3+}. Figure S4 displayed that the M_2@TA-Eu particles exhibited rapid heating effect even after repeated laser irradiations, and the temperature could be raised to ~65ºC in each irradiation at a fixed concentration (500 μg/mL). Further, the good photothermal responsiveness of MXenes allowed the M@TA-Eu particles to exhibit sensitive photothermal response under multi-wavelength solar radiation. As shown in Figure 1h, the M_2@TA-Eu particles could be heated to ~38ºC under solar radiation, showing the sensitivity of the particle's photothermal response. The above results implied that the embedding of MXenes gives the material good photothermal responsiveness.

3.3 Antioxidant activity of M@TA-Eu particles

The accumulation of excess reactive oxygen species in the wound due to the harsh seawater environment is one of the factors that induce difficult healing of the wound. Natural small molecule antioxidants have been shown to be effective molecules in scavenging wound ROS [39]. Due to the presence of the phenolic hydroxyl, TA can easily release protons and show good antioxidant properties. As shown in Figure2a&b, based on the good antioxidant properties of TA, all the particles showed up to 90% scavenging efficiency against DPPH radicals. And the characteristic absorption peaks of DPPH radicals at 517 nm in the UV-vis spectra showed correspondingly reduced. Also, the particles displayed good scavenging effect on other types of reactive oxygen radicals, including H_2O_2 and $\bullet O_2^-$ (Figure 2c&d). Among them, the inhibition of $\bullet O_2^-$ was slightly improved by the introduction of MXenes, which may be caused by the conductivity of MXenes allowing faster electron transfer during the oxidation process [40, 41]. Moreover, the particles also had an effective scavenging capacity for intracellular ROS (Figure 2e). H_2O_2 generated a large number of free radicals in cells, which exhibited

an intense green fluorescence. The weakening of intracellular fluorescence intensity after co-incubation with the particles confirmed the scavenging of ROS. These results show that the M@TA-Eu particles were capable of scavenging a wide range of free radicals and could mitigate cellular damage from ROS.

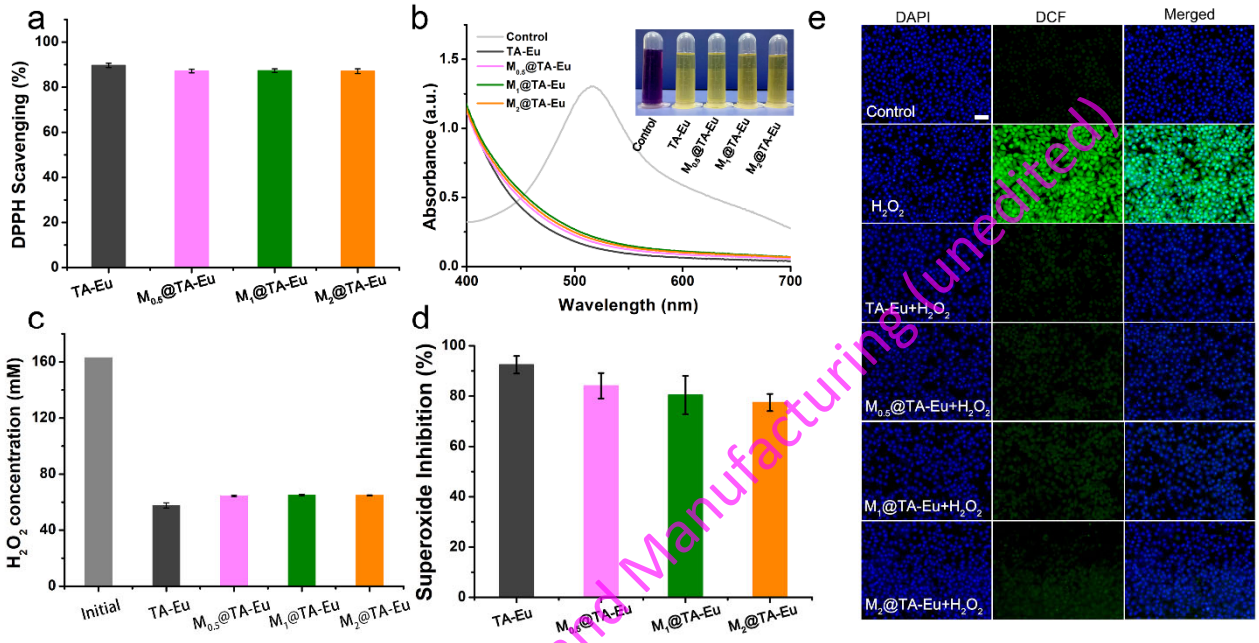

Figure 2 DPPH radical scavenging activity (a) and UV-Vis absorption spectra (b) after scavenging by M@TA-Eu particles; H_2O_2 scavenging (c) and superoxide anions inhibition (d) by the M@TA-Eu particles; Fluorescence images of intracellular ROS in L929 cells exposed to the M@TA-Eu particles (e, scale bars: 40 μm).

3.4 Cellular compatibility of the M@TA-Eu particles

Bio-safety of wound dressing is a key index for their application. The cellular compatibility of the M@TA-Eu was evaluated by detecting the effect of the particles on cell viability and proliferation. Here, we first screened the optimal incubation concentration by incubating HUVEC cells with different concentrations of M1@TA-Eu particles, which was used to avoid dose toxicity of M@TA-Eu particles to cells. The HUVEC cells exposed to the different concentrations of the M_1@TA-Eu particles exhibit

different proliferation activity (Figure S5a). Specifically, the low concentrations (< 0.1 mg/mL) of the M_1@TA-Eu particles exhibited effective pro-proliferative effects on the HUVEC cells. In contrast, particles at high concentrations (> 0.5 mg/mL) exhibited dose-dependent toxicity on cell proliferation. Therefore, we selected M@TA-Eu particles at a concentration of 0.05 mg/ml to further investigate the effect on cell proliferation and viability. As shown in Figure 3a, all particles effectively promoted HUVEC cells proliferation, even in the M_2@TA-Eu group that loaded with high dose of MXenes. The pro-proliferative effect of the M@TA-Eu particles on cells is mainly due to the beneficial stimulation of cell proliferation by TA and Eu element [21, 42]. The slow-release experiment showed that both TA and Eu^{3+} can be effectively released from the particles (Figure S5b, c&d). Due to the competition for phenolic hydroxyl groups between hydrogen protons and Eu^{3+}, the particles displayed more release of TA and Eu^{3+} in weakly acidic wound environments[43]. Additionally, based on the weak interaction between MXenes, TA, and Eu^{3+}, the release concentration of TA and Eu^{3+} decreased with the increase of MXenes doping amount. As functional components, the release of TA and Eu^{3+} could improve cell viability, which served as the foundation for improving wound healing in real time[44]. In addition, the fluorescence images of AO/EB staining displayed the safety of the M@TA-Eu particles on HUVEC cells (Figure 3b). Similarly, the M@TA-Eu particles were able to promote L929 cells proliferation safely and effectively (Figure 3c&d). Moreover, the hemocompatibility of the M@TA-Eu particles was tested to assess their ability to destroy blood cells. The good hemocompatibility of the wound dressing will avoid systemic side effects caused by the rupture of a large number of blood cells. As displayed in Figure S6, the hemolysis ratios of the M@TA-Eu particles exhibited a negligible hemolysis rate of 0.3-0.4%, showing good hemocompatibility [45]. The above results revealed that the good cytocompatibility and hemocompatibility of the M@TA-Eu particles.

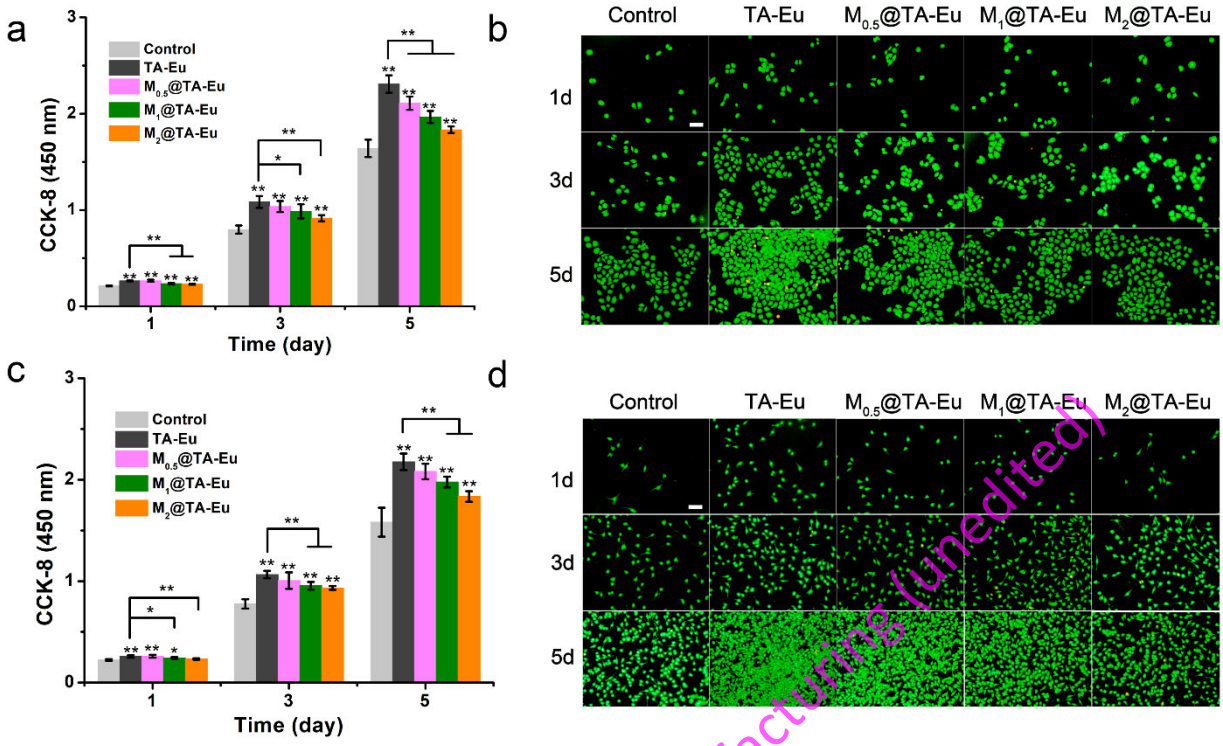

Figure 3 Effect of the M@TA-Eu (0.05 mg/mL) complexes on the proliferation of HUVECs (a) and L929 (c); Fluorescence images of HUVECs (b) and L929 (d) after AO/EB staining at different times (1, 3, and 5 days, scale bars: 20 μm).

3.5 Bactericidal performance of the M@TA-Eu particles

Bacterial infection is a major impediment to wound healing, which makes bactericidal function one of the key properties of wound dressings. In this work, the bactericidal performance of the M@TA-Eu particles was evaluated. The inherent antimicrobial properties of TA and MXenes allowed the M@TA-Eu particles to have certain antimicrobial properties, especially against Gram-positive bacteria (Figure 4c, *S.aureus*) [46, 47]. However, this antibacterial effect was not ideal in wound healing. In addition, the antibacterial capacity of TA against Gram-negative species that predominate in seawater was insufficient (Figure 4a) [48]. The intolerance of bacteria to high temperatures provided an effective strategy for efficient bacterial killing. Here, the photothermal effect of the M@TA-Eu particles was

expected to further provide sufficient bactericidal function. As shown in Figures 4b&d, NIR irradiation did not change the antibacterial activity of Control and TA groups. Significantly, NIR-assisted M@TA-Eu particles displayed a significant enhancement in antimicrobial activity. Among them, the NIR-assisted killing efficiency of the M_2@TA-Eu against both Gram-negative and Gram-positive bacteria was close to 98%.

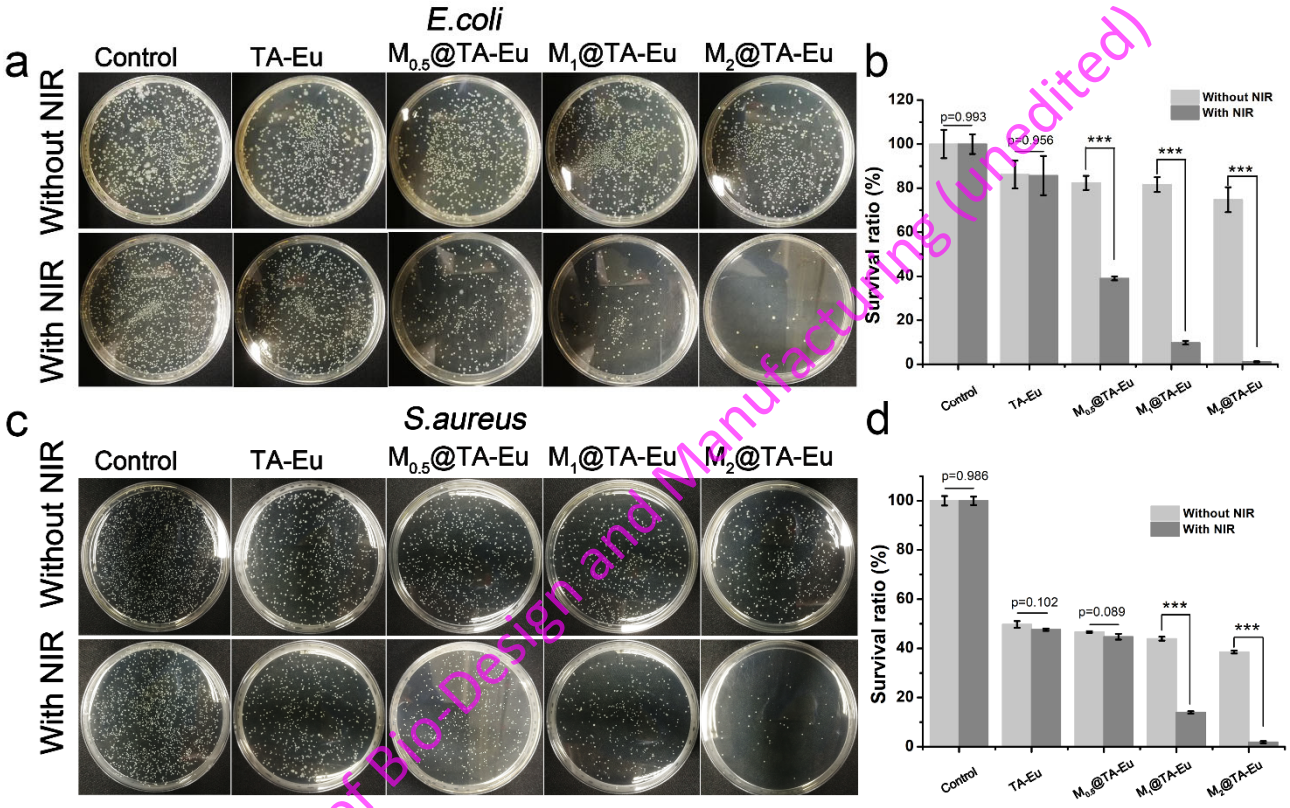

Figure 4 Antibacterial performance of the M@TA-Eu particles with/without NIR light irradiation. (a, c): photographs of bacterial colonies of *E. coli* and *S. aureus* incubated with the M@TA-Eu particles with/without NIR light; (b, d): bacterial survival rate of *E. coli* and *S. aureus* incubated with the M@TA-Eu particles with/without NIR light (n=3 for statistical data, ***represents $p < 0.001$ between the selected groups).

The morphology of the bacteria after treatment with the particles was observed. The *E.coli* exhibited a smooth rod-like morphology with intact cell membrane in the control group with or without NIR

irradiation, indicating that the NIR irradiation had little effect on the cell membrane structure (Figure S7). Also, *E. coli* showed a small amount of individual damage in the M@TA-Eu groups without NIR irradiation, indicating the limited killing power of the M@TA-Eu particles. In comparison, the photothermal treatment composed by the M@TA-Eu and NIR irradiation caused severe folding of the cell membrane, which resulted in substantial damage to the bacteria. Also, similar results were observed for bactericidal properties against *S.aureus*. The antibacterial properties of M@TA-Eu particles are mainly attributed to the photothermal response triggered by the MXenes. Also, as the multidentate ligands, the interaction of TA to the proteins of bacteria aids the antibacterial properties of the M@TA-Eu particles [49, 50]. The above results confirmed that the outstanding photothermal response of MXenes conferred efficient photothermal bactericidal properties on the M@TA-Eu particles.

3.6 Wound healing

3.6.1 Wound closure

An SD rat model of infected seawater immersion wound was established to evaluate the effectiveness of the M@TA-Eu particles with NIR irradiation in promoting wound healing. On Day 3, the control group still showed purulent infection compared with the group with no seawater immersion, indicating severe infection of the wound (Figure 5a). In contrast, a tendency to scab was observed in the group without no seawater immersion. Also, all M@TA-Eu particles treated groups showed an accelerated wound healing process, especially M_2@TA-Eu+NIR group. On Day 11, M_2@TA-Eu+NIR group was close to healing and showed a repair effect close to that of the group with no seawater immersion. In the process of wound healing, the M_2@TA-Eu+NIR all exhibited the highest wound healing rate at all time points (Day3: ~16.1%, Day7: ~71.2%, and Day11: ~90.3%, Figure 5b). The

results suggested that the M2@TA-Eu particles assisted by NIR could promote the healing of infected seawater immersion wounds.

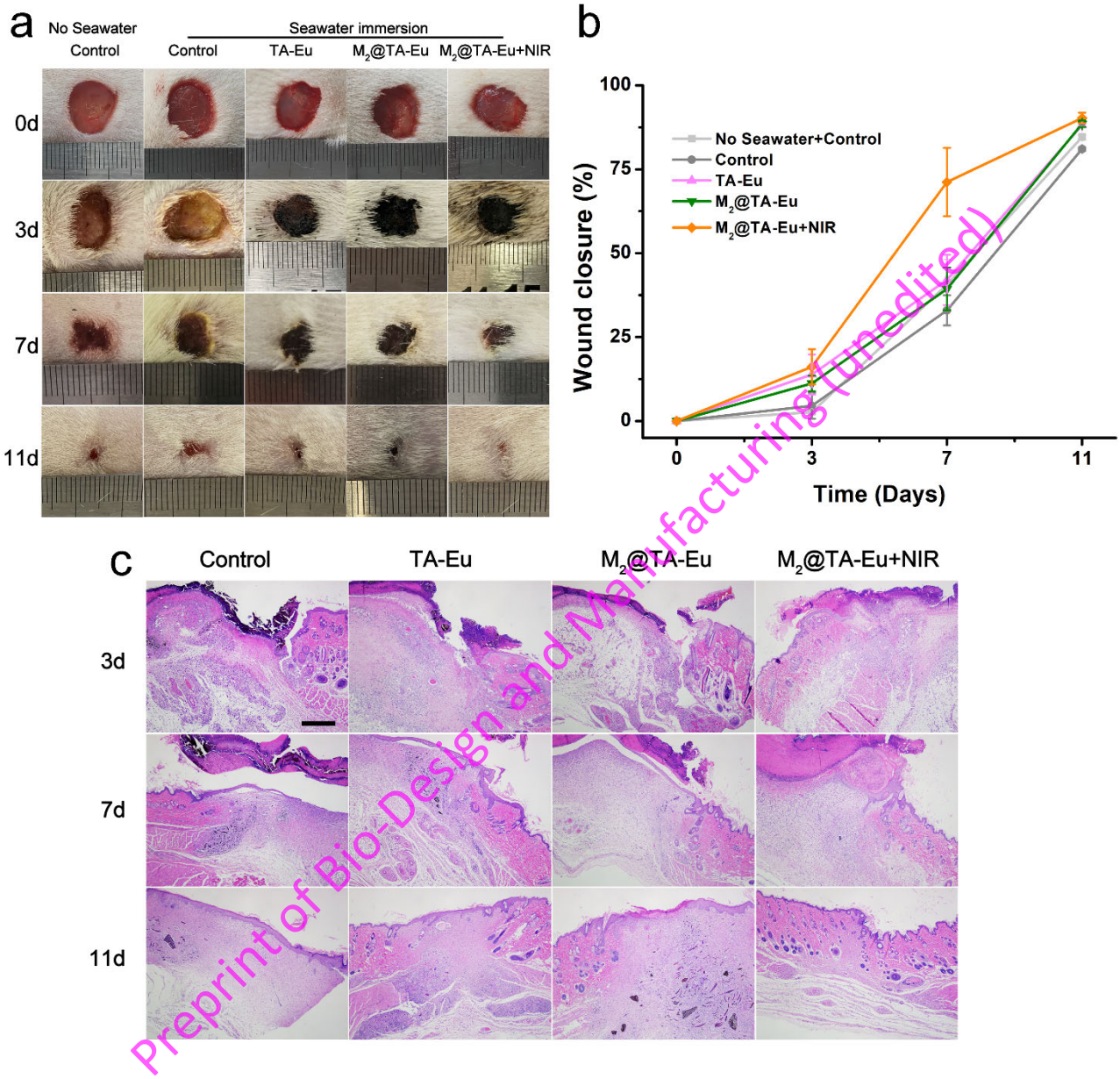

Figure 5 Digital photos of wound healing after treated with M@TA-Eu particles at different times (a), and the corresponding ratio of wound closure (b); H&E staining of the wound at 3, 7, and 11 days (c) (scale bars: 500 μm).

3.6.2 Histological analysis

Wound healing is a complex process in which multiple cells work together, including inflammation,

proliferation, and remodeling phases. H&E staining was employed to observe the wound repair process (Figure 5c). On Day 3, groups treated with the particles showed weaker inflammatory cell infiltration compared with the control group. Among them, the M_2@TA-Eu+NIR group displayed partial epidermal regeneration. On Day 7 after surgery, all groups showed partial regeneration of epithelialization, suggesting an accelerated repair process. Especially, the groups treated with the particles showed more intact regenerating epithelium as well as the regeneration of skin appendages, including blood vessels and hair follicles. Among them, the M_2@TA-Eu+NIR group possessed optimal epidermal-dermal junction that was the upward projections of the papillary dermis and corresponding downward projections of the epidermis. On Day 11, more skin appendages were observed in the M_2@TA-Eu+NIR group, indicating a good recovery of the skin tissue.

Collagen deposition is an important feature of wound healing. Masson's staining was used to evaluate the collagen deposition in the wound at different time periods (Figure S8). On Day 3, all groups observed significant interstitial edema and structural disorders. On Day 7, the groups treated with the particles were first to show more collagen deposition and more ordered organizational structure. On Day 11, group M_2@TA-Eu+NIR had more collagen deposition and a more ordered structure compared with other groups. These results revealed that the NIR-assisted M_2@TA-Eu could inhibit inflammatory cell aggregation and promote granulation growth and collagen deposition.

3.6.3 Immunohistochemistry analysis

Inflammatory response is an important stage in the wound healing process. Here, the immunohistochemical analysis was employed to evaluated the inflammatory changes in wounds. As the pro-inflammatory cytokines, IL-1β and IL-6 were used to mark the inflammatory condition at the wound sites [51, 52]. And all the M@TA-Eu particles groups inhibited the expression of IL-1β and IL-

6 during the initial phase of repair (Figure 6a&b). Among them, M_2@TA-Eu+NIR showed the most significant inhibition effect. Also, as an anti-inflammatory factor, the expression of TGF-β1 at the wound sites on day 3 was examined [53]. As shown in Figure 6c, the positive expression of TGF-β1 cytokines in the M_2@TA-Eu+NIR group was more significant compared with other groups. The suppression of excessive inflammation accelerated regeneration of new tissue and provided a more healing-friendly environment for wounds [54]. These results indicated that NIR-assisted M_2@TA-Eu could promote wound healing by modulating inflammation in the early stages of wound healing.

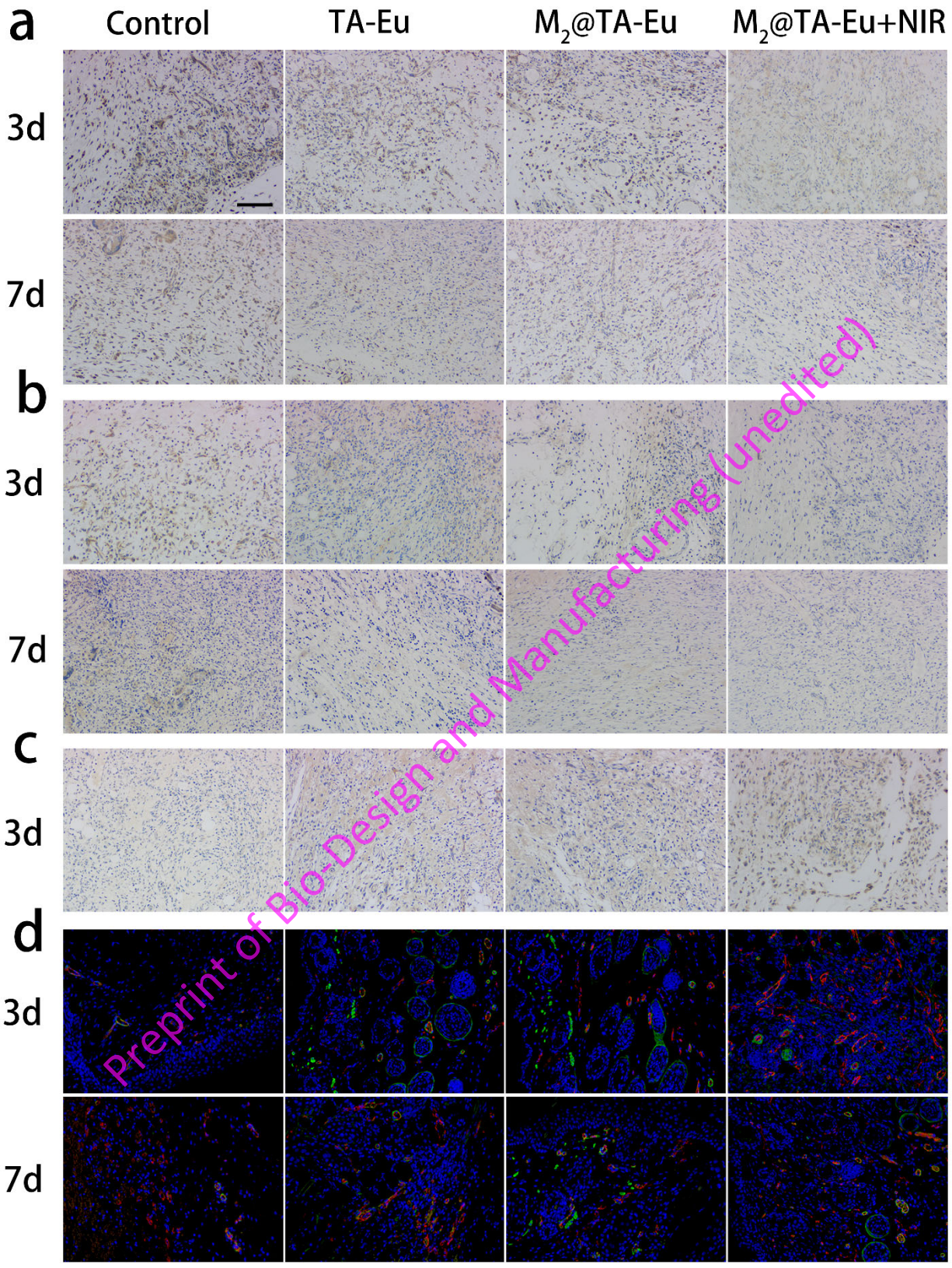

Figure 6 Immunohistological staining of IL-1β (a), IL-6 (b), TGF-β1 (c), CD31(red) and α-SMA (green) (d) on wound sites at different times (scale bar: 100 μm).

The regeneration of blood vessels during the healing process is crucial for the delivery of oxygen and nutrients. Timely vascular regeneration is necessary for wound healing. As shown in Figure 6d, the expression of CD31 and α-SMA, representing the neovascularization and smooth muscle cells, was examined at the wound sites [55]. On Day 7 after surgery, the groups treated with the particles had significant vascular regeneration compared with control group. Especially, the M_2@TA-Eu+NIR group displayed substantial vascular regeneration. On Day 11, control group showed improved vascularization, while the trend of diminished vascularization was observed in other groups. A large amount of immature vascular tissue will form temporarily in the wound to promote rapid healing, additionally, they will degenerate in time after the wound is healed to avoid excessive wound proliferation [56]. The above results revealed that NIR-assisted M_2@TA-Eu could improve the vascularization of wounds. In addition, the NIR-assisted M_2@TA-Eu could effectively intervene in the inflammatory and proliferative phases of the wound process to accelerate healing.

3.6.4 Bacterial colonization of the wound site

The bacterial colonization at the wound sites was also detected to assess the effectiveness of the bactericidal effect of particles. Here, the bacterial colonization of each wound site was examined after 3 days of treatment. Specifically, the wound tissue was collected and homogenized in normal saline (3 mL). After serial dilutions, *S. aureus, E. coli, and P. aeruginosa* were obtained by screening. After taking the corresponding bacterial solution (100 μL) for plate culture, the colony growth of the wound was recorded to evaluated the antimicrobial properties of particles in wounds. As shown in Figure 7, the control group with seawater immersion displayed a large amount of bacterial colonization. In contrast, the TA-Eu and M_2@TA-Eu groups displayed partial bacterial removal, but a large number

of bacteria were still alive, especially Gram-negative species. The NIR-assisted M_2@TA-Eu group demonstrated a similar antimicrobial effect to the group with no seawater immersion (uninfected), which confirmed that NIR-assisted M_2@TA-Eu fought infection by rapidly killing bacteria in the early stages of infected wound to accelerate wound healing. In general, the timely killing of wound bacteria provided the condition for the subsequent presentation of bacterial antigens by particles.

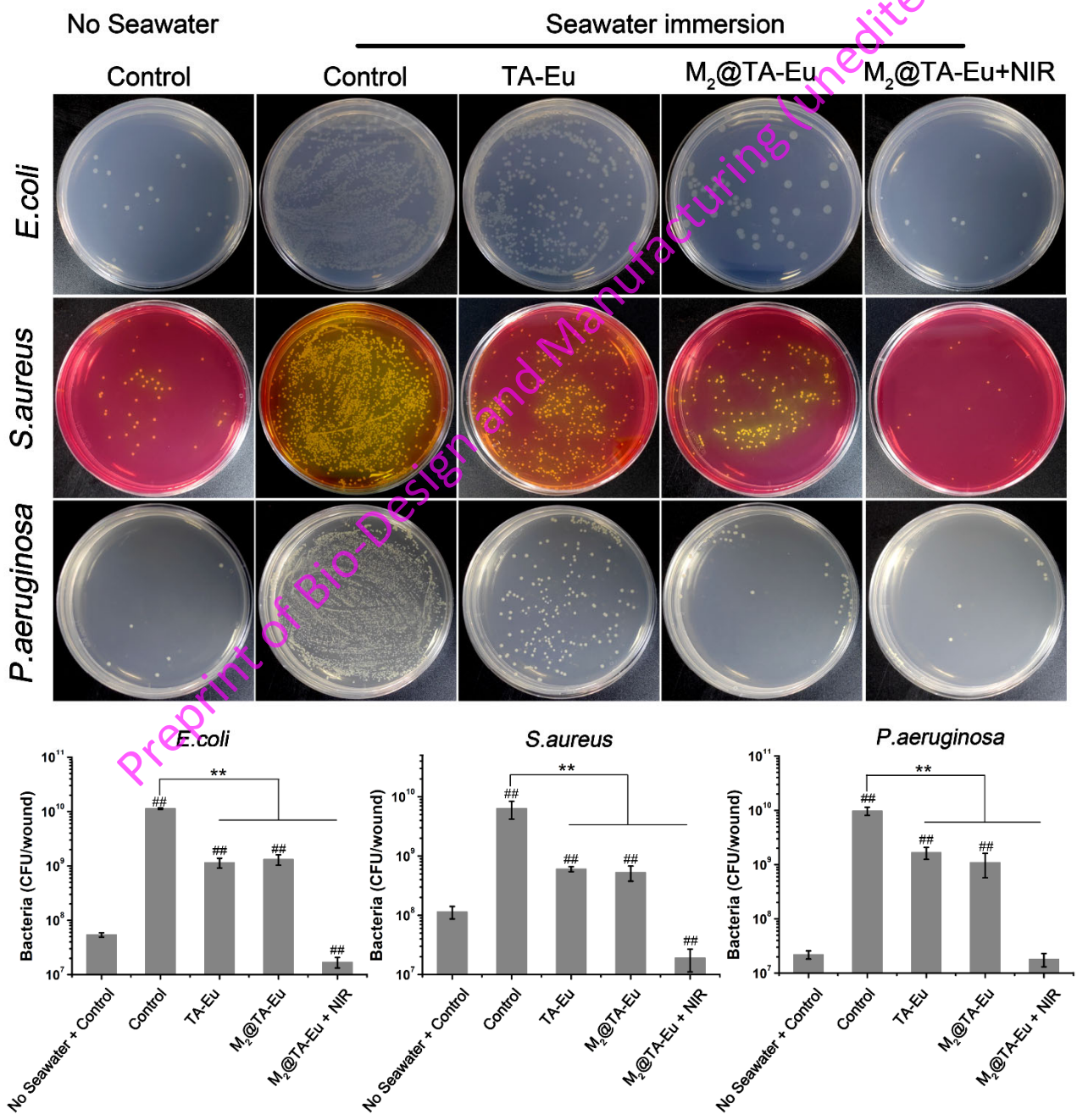

Figure 7 On day 3, the colony growth and statistics of each wound (n=3 for statistical data, ##$p < 0.01$ vs No seawater + Control, ** represents $p < 0.01$ between the selected groups).

3.7 Efficacy of the formed in situ vaccines

3.7.1 Antigen presentation and maturation of DCs

In a classical immune response, the invasion of pathogens would trigger host immune system, and their antigen signals need to be presented by APCs to the lymphocytes residing in the secondary lymph organs such as spleens and lymph nodes. DCs are the most important and professional APCs, which usually patrol the peripheral tissues for capturing invading pathogens. After that, the DCs need to internalize, digest, process the pathogens to antigen peptides, and the present the antigen peptides to the lymphocytes via two types of presentation molecules, the class II major histocompatibility complex (MHC II) and the class I major histocompatibility complex (MHC I) molecules. Generally, exogenous antigens are presented via MHC II molecules to $CD4^+$ T lymphocytes to trigger humoral immune responses. At the same time, the maturation of DCs is another indispensable step for the antigen presentation, the feathers of which include the high expression of costimulatory molecules CD40, CD80, and CD86 on DCs surface.

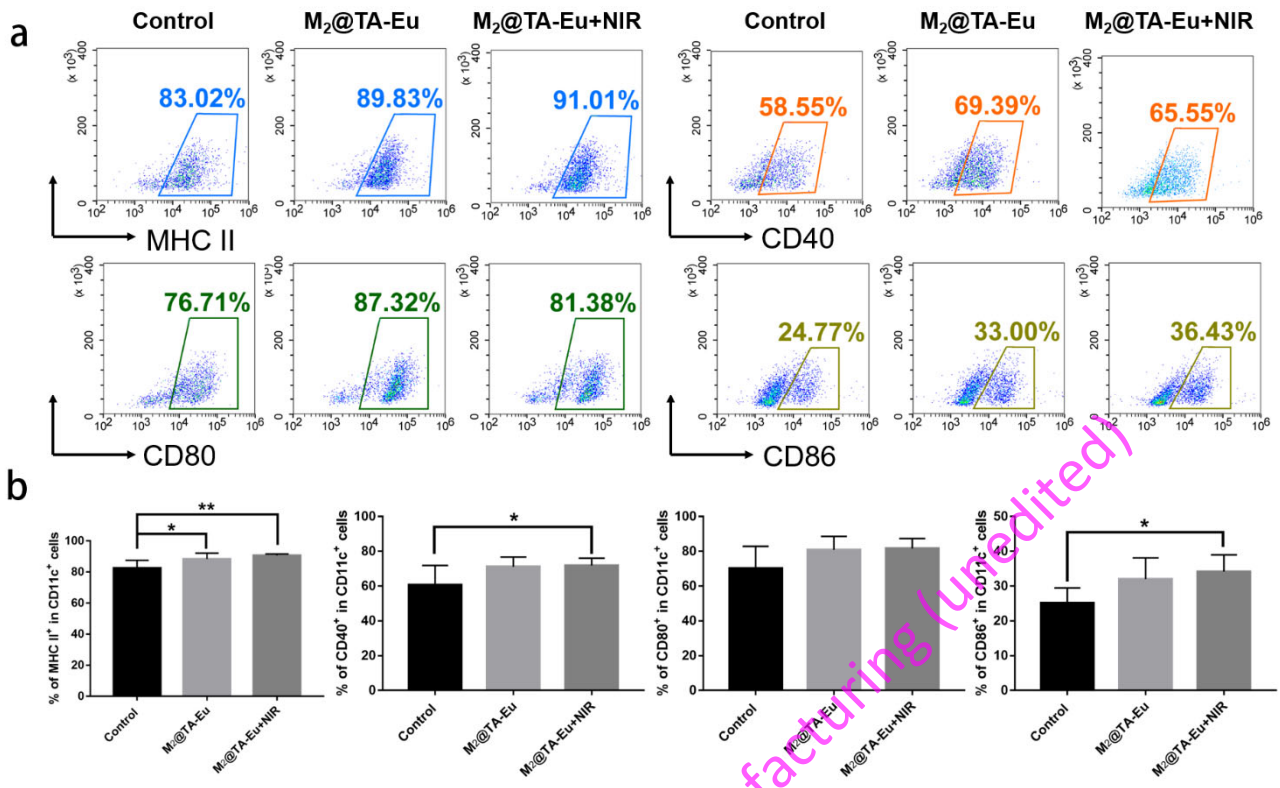

Figure 8 On the 2nd day after vaccination, the expression of MHC II, CD40, CD80 and CD86 on $CD11c^+$ DCs as detected by flow cytometry. Representative flow charts of each group (a). The percentage of MHC II, CD40, CD80 and CD86 molecules expressed on $CD11c^+$ DC cells (b). (n=5 for statistical data, * and ** represent $p < 0.05$ and $p < 0.01$ between the selected groups)

Here, we detected the expression levels of the MHC II and costimulatory molecules on $CD11c^+$ among the lymphocytes collected from the rats. As shown in Figure 8, the MHC II expressions of the M_2@TA-Eu and M_2@TA-Eu+NIR groups were both significantly higher than that of the control group. The CD40 expression of the M_2@TA-Eu+NIR group was significantly higher than that of the control group. The CD80 expressions of the M_2@TA-Eu and M_2@TA-Eu+NIR groups were both higher than that of the control group. The CD86 expression of the M_2@TA-Eu+NIR group was significantly higher than that of the control group. These results indicate that the treatment with the M_2@TA-Eu + NIR

significantly promoted the MHC II-mediated antigen presentation and maturation of the DCs, which could further enhance the humoral immune response to the invaded pathogenic bacteria. The promotion should be attributed to the photothermal effect of the M_2@TA-Eu particle, as previous literatures reported that localized mild photothermal effects (~45℃) can stimulate immune response by multiple mechanisms, including recruitment and activation of APCs, and adjusting local microenvironment [57, 58]. In addition, the expression levels of the MHC II and costimulatory molecules of the M_2@TA-Eu group were collectively higher than the control group. This may be attributed to enhanced antigen presentation by the interaction of TA with intracellular proteins after bacterial death [20].

3.7.2 Antibody production and cytokines secretion at 7th day after the vaccination

Humoral immunity plays an essential role in fighting bacteria infection by producing antibodies, which can inactivate or eliminate the invaded bacteria via different ways. Therefore, antibody titer is an indicator of the level of humoral immune response toward bacteria infection. Here, we detected the antibody IgG titer in the sera and the secretion levels of the cytokines by the re-stimulated splenocytes of the rats 7 days after the bacteria infection. From Figure 9a, the total IgG titer against the three bacteria of the M_2@TA-Eu+NIR group was significantly higher than those of the M_2@TA-Eu and control group. Specifically, the IgG titer against the *E. coli* of the M_2@TA-Eu+NIR group was higher than those of the M_2@TA-Eu and control group. The IgG titer against the *S. aureus* of the M_2@TA-Eu+NIR group was higher than those of the M_2@TA-Eu and control group. The IgG titer against the *P. aeruginosa* of the M_2@TA-Eu+NIR group was higher than those of the M_2@TA-Eu and control group. These results indicate that the treatment with M_2@TA-Eu+NIR induced higher level of the bacteria-specific IgG titer.

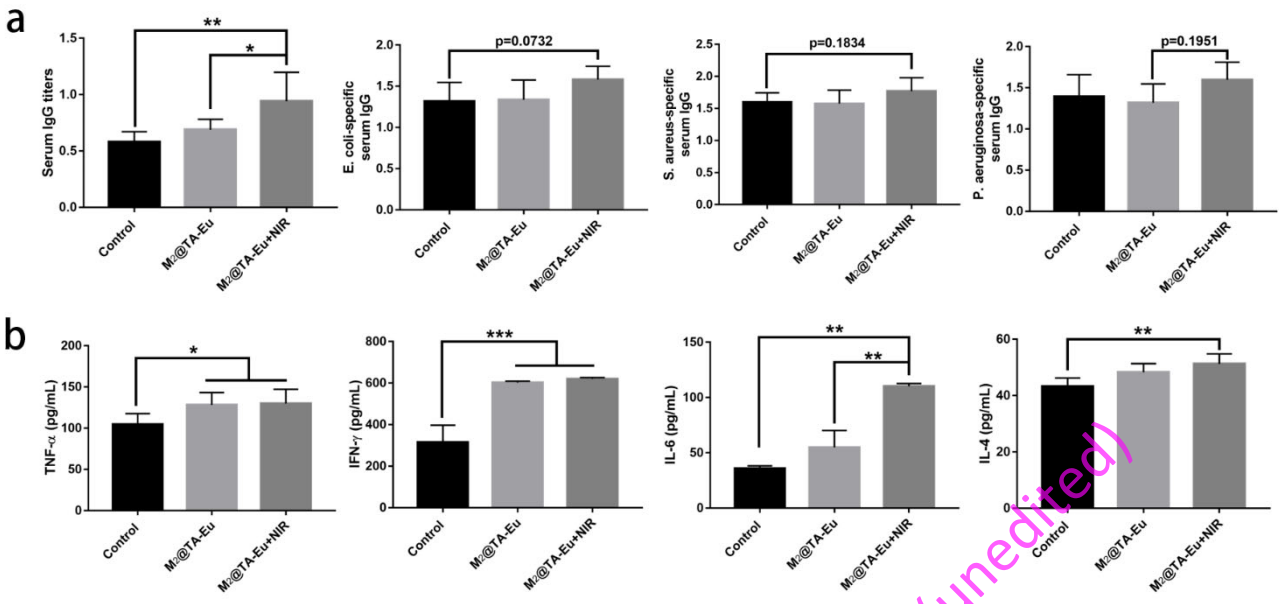

Figure 9 Serum IgG titers and cytokine levels on the 7th day after vaccination. Total IgG titer against the three bacteria, *E. coli*-specific IgG titer, *S. aureus*-specific IgG titer, and P. aeruginosa-specific IgG titer in the sera (a). Levels of the cytokines TNF-α, IFN-γ, IL-6, and IL-4 secreted by the restimulated splenocytes (b). (n=5 for statistical data *, **, and *** represent $p < 0.05$, $p < 0.01$, and $p < 0.001$ between the selected groups).

In addition, the cytokines secreted by the splenocytes also indicate the intensity and type of the immune response toward bacteria infection. Mature DCs present antigens to $CD4^+$ and/or $CD8^+$ splenocytes to further induce humoral and/or cellular immunity. Then, Th1 subset of $CD4^+$ splenocytes secrete the cytokines such as IFN-γ and TNF-α to promote cellular immunity. Th2 subset of $CD4^+$ splenocytes secrete the cytokines such as IL-4, IL-6 and IL-10 to promote humoral immunity [59]. From Figure 9b, the TNF-α and IFN-γ levels of the M_2@TA-Eu and M_2@TA-Eu + NIR groups were both significantly higher than that of the control group. The IL-6 level of the M_2@TA-Eu + NIR group was significantly higher than those of the M_2@TA-Eu and control group. The IL-4 level of the M_2@TA-Eu + NIR group was significantly higher than that of the control group. From the results, the treatment with M_2@TA-Eu + NIR could promote both the humoral and cellular immunity toward the

infected bacteria.

3.7.3 Antibody levels at 40th day after the vaccination

To further detect the duration of the immune response along with time, we detected the antibody IgG titer in the sera of the rats 40 days after the bacteria infection. From Figure 10a, the total IgG titer against the three bacteria of the M_2@TA-Eu + NIR group was higher than those of the M_2@TA-Eu and control group. Specifically, the IgG titer against the *E. coli* of the M_2@TA-Eu + NIR group was higher than those of the M_2@TA-Eu and control group. The IgG titer against the *S. aureus* of the M_2@TA-Eu + NIR group was higher than that of the control group. The IgG titer against the *P. aeruginosa* of the M_2@TA-Eu + NIR group was higher than those of the M_2@TA-Eu and control group. These results indicate that the treatment with M_2@TA-Eu + NIR induced long-term bacteria-specific IgG titer, which could fight the bacteria infection for a long time.

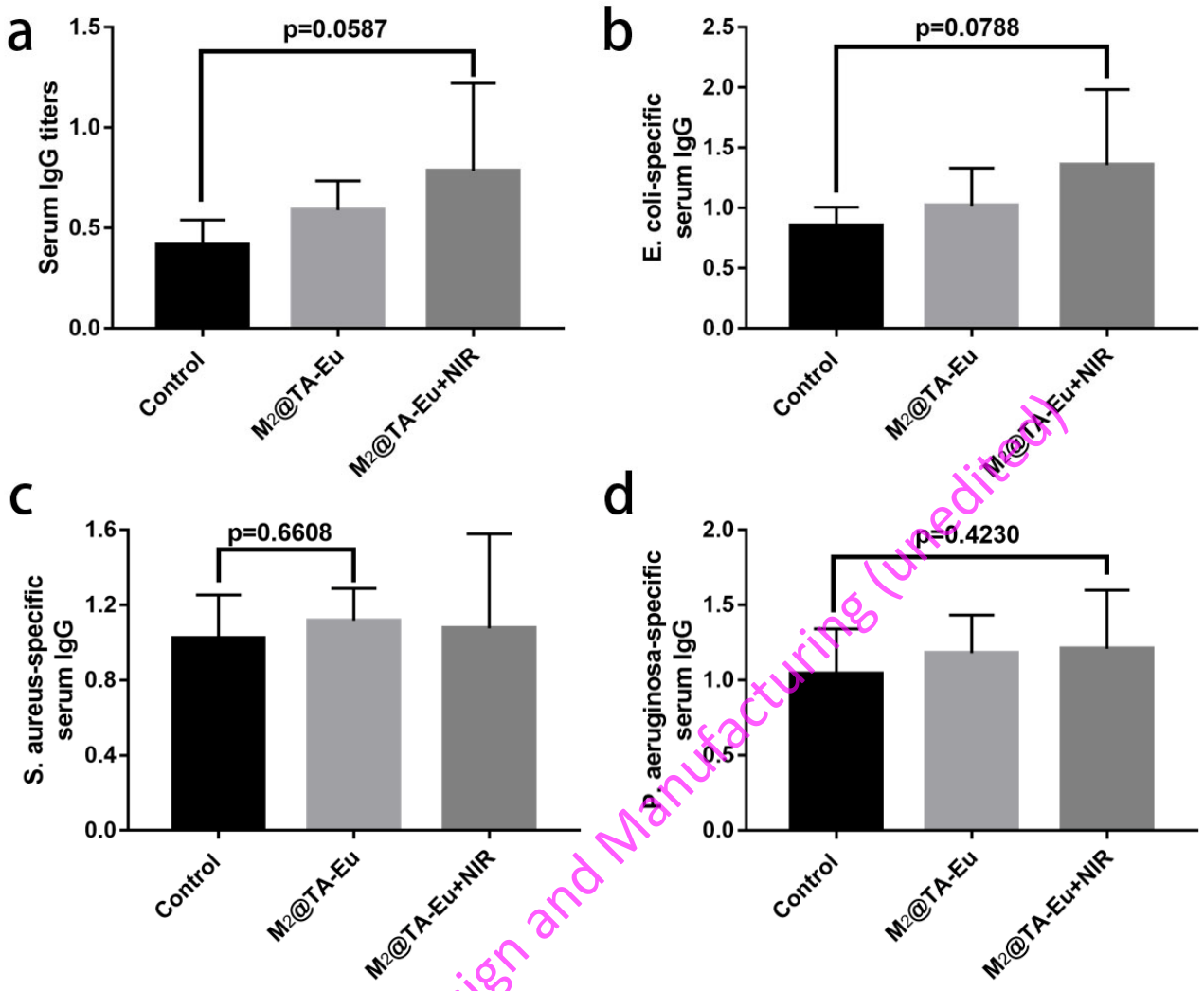

Figure 10 IgG titers on the 40th day after the vaccination. Total serum IgG titer against the three bacteria (a), and the serum IgG titers specific to *E. coli* (b), *S. aureus* (c) or *P. aeruginosa* (d). (n=5 for statistical data, * and *** represent $p < 0.05$ and $p < 0.001$ between the selected groups)

4 Conclusions

In summary, in the face of complex and refractory infected seawater immersion wound, a simple, efficient, and biocompatible particles (M@TA-Eu) were prepared by embedding the MXenes into the polyphenol-metal composite particles and used to accelerate the repair of wound by assist the organism in achieving a long-lasting anti-infection immune mechanism. The results displayed that the

embedding MXenes endowed the particles with good photothermal response ability. This allowed the M@TA-Eu particles to exhibit good bactericidal properties as well as the potential to enhanced vaccination efficacy. Also, the functional platform constructed by TA and Eu^{3+} had the characteristics of antioxidation, promoting angiogenesis, and promoting antigen presentation. Moreover, the M@TA-Eu particles possessed good cytocompatibility and hemocompatibility. Furthermore, the animal experiments display that the NIR-assisted M_2@TA-Eu particles could effectively kill the invaded bacteria, inhibit wound inflammation, and promote angiogenesis, achieving a multi-stage promotion of healing from the inflammatory and proliferative phases. Particularly, the NIR-assisted M_2@TA-Eu particles produced potent vaccination effect by forming in situ bacterial vaccines, which constructed a long-lasting anti-infection mechanism for refractory infected wounds. Therefore, the NIR-assisted M@TA-Eu particles may be a simple and promising wound dressing for the infected seawater immersion wound.

Author contribution

Zhentao Li: Investigation, Methodology, Data curation, Writing – original draft. **Ting Song**: Methodology, Investigation. **Yanpeng Jiao**: Investigation, Software, Funding acquisition. **Yang Liao**: Investigation, Methodology. **Zonghua Liu**: Conceptualization, Supervision, Writing – review & editing.

Conflicts of interest

There are no conflicts of interest to declare.

Acknowledgements

This work was supported by National Key Research and Development Program of China (grant no. 2018YFC0311103), Project of Science and Technology Innovation Cultivation for University Students

of Guangdong Province (grant no. pdjh202010062), Science and Technology Project of Guangzhou City (grant no. 2018020100), General Program of China Postdoctoral Science Foundation (grant no. 2021M701599), National Natural Science Foundation of China (grant no. 32201083), the Science and Technology Program of Heyuan, China (230510171473326), the Science and Technology Program of Guangzhou, China (2024A03J0232), Medical Scientific Research Foundation of Guangdong Province of China (A2020548), and the Fundamental Research Funds for the Central Universities, China (21623403).

References

[1] B. Shi, J. Sun, Y. Cao, F. Yang, Y. Wu, X. Liang, L. Li, Application of vacuum sealing drainage to the treatment of seawater-immersed blast-injury wounds, Int Wound J 13(6) (2016) 1198-1205.
[2] X. Wang, P. Xu, Z. Yao, Q. Fang, L. Feng, R. Guo, B. Cheng, Preparation of Antimicrobial Hyaluronic Acid/Quaternized Chitosan Hydrogels for the Promotion of Seawater-Immersion Wound Healing, Front Bioeng Biotechnol 7 (2019) 360.
[3] H. Yan, Q. Mao, Y. Ma, L. Wang, X. Chen, Y. Hu, H. Ge, Seawater immersion aggravates burn injury causing severe blood coagulation dysfunction, BioMed research international 2016 (2016).
[4] A.J. Bullock, M. Garcia, J. Shepherd, I. Rehman, M. Sheila, Bacteria induced pH changes in tissue-engineered human skin detected non-invasively using Raman confocal spectroscopy, Applied Spectroscopy Reviews 55(2) (2020) 158-171.
[5] Q. Fang, Z. Yao, L. Feng, T. Liu, S. Wei, P. Xu, R. Guo, B. Cheng, X. Wang, Antibiotic-loaded chitosan-gelatin scaffolds for infected seawater immersion wound healing, Int J Biol Macromol 159 (2020) 1140-1155.
[6] J. Huo, Q. Jia, H. Huang, J. Zhang, P. Li, X. Dong, W. Huang, Emerging photothermal-derived multimodal synergistic therapy in combating bacterial infections, Chemical Society Reviews (2021).
[7] Q. Jia, Q. Song, P. Li, W. Huang, Rejuvenated photodynamic therapy for bacterial infections, Advanced healthcare materials 8(14) (2019) 1900608.
[8] Y. Liu, F. Li, Z. Guo, Y. Xiao, Y. Zhang, X. Sun, T. Zhe, Y. Cao, L. Wang, Q. Lu, Silver nanoparticle-embedded hydrogel as a photothermal platform for combating bacterial infections, Chemical Engineering Journal 382 (2020) 122990.
[9] K. Bruggeman, M. Zhang, N. Malagutti, S. Soltani Dehnavi, R. Williams, A. Tricoli, D. Nisbet, Using UV-Responsive Nanoparticles to Provide In Situ Control of Growth Factor Delivery and a More Constant Release Profile from a Hydrogel Environment, ACS Applied Materials & Interfaces 14(10) (2022) 12068-12076.
[10] Y. Zhang, S. Ma, X. Liu, Y. Xu, J. Zhao, X. Si, H. Li, Z. Huang, Z. Wang, Z. Tang, Supramolecular assembled programmable nanomedicine as in situ cancer vaccine for cancer immunotherapy, Advanced Materials 33(7) (2021) 2007293.
[11] R.H. Pierce, J.S. Campbell, S.I. Pai, J.D. Brody, H.E. Kohrt, In-situ tumor vaccination: bringing the fight to the tumor, Human vaccines & immunotherapeutics 11(8) (2015) 1901-1909.
[12] H. Lin, C. Yang, Y. Luo, M. Ge, H. Shen, X. Zhang, J. Shi, Biomimetic nanomedicine-triggered in situ vaccination

for innate and adaptive immunity activations for bacterial osteomyelitis treatment, ACS nano 16(4) (2022) 5943-5960.
[13] M.A. Luzuriaga, F.C. Herbert, O.R. Brohlin, J. Gadhvi, T. Howlett, A. Shahrivarkevishahi, Y.H. Wijesundara, S. Venkitapathi, K. Veera, R. Ehrman, Metal–organic framework encapsulated whole-cell vaccines enhance humoral immunity against bacterial infection, ACS nano 15(11) (2021) 17426-17438.
[14] J. Zhu, R. Chang, B. Wei, Y. Fu, X. Chen, H. Liu, W. Zhou, Photothermal Nano-Vaccine Promoting Antigen Presentation and Dendritic Cells Infiltration for Enhanced Immunotherapy of Melanoma via Transdermal Microneedles Delivery, Research 2022 (2022).
[15] Y. Li, L. He, H. Dong, Y. Liu, K. Wang, A. Li, T. Ren, D. Shi, Y. Li, Fever-Inspired Immunotherapy Based on Photothermal CpG Nanotherapeutics: The Critical Role of Mild Heat in Regulating Tumor Microenvironment, Advanced Science 5(6) (2018) 1700805.
[16] F. Cao, M. Yan, Y. Liu, L. Liu, G. Ma, Photothermally controlled MHC class I restricted CD8+ T-cell responses elicited by hyaluronic acid decorated gold nanoparticles as a vaccine for cancer immunotherapy, Advanced healthcare materials 7(10) (2018) 1701439.
[17] S.S. Said, S. Campbell, T. Hoare, Externally addressable smart drug delivery vehicles: current technologies and future directions, Chemistry of Materials 31(14) (2019) 4971-4989.
[18] Y. Li, R. Fu, Z. Duan, C. Zhu, D. Fan, Construction of multifunctional hydrogel based on the tannic acid-metal coating decorated MoS2 dual nanozyme for bacteria-infected wound healing, Bioactive Materials 9 (2021) 461-474.
[19] B. Molina-Ramírez, N. Cabral-Hipólito, I. Castillo-Maldonado, D. Delgadillo-Guzmán, R. Meza-Velázquez, A. Ramírez-Moreno, E. Flores-Loyola, P. Ruíz-Flores, J.H.-S. Cruz, P.-K. Espino-Silva, Tannic Acid, as a Structural Moiety Coupled to a Protein Antigen, Exhibiting a Molecular-structure Adjuvant Activity for Antibody Specificity Enhancement, Protein and Peptide Letters 29(11) (2022) 925-936.
[20] S. Madrigal-Carballo, L. Haas, M. Vestling, C.G. Krueger, J.D. Reed, Non-covalent pomegranate (Punica granatum) hydrolyzable tannin-protein complexes modulate antigen uptake, processing and presentation by a T-cell hybridoma line co-cultured with murine peritoneal macrophages, International journal of food sciences and nutrition 67(8) (2016) 960-968.
[21] M. Luo, M. Wang, W. Niu, M. Chen, W. Cheng, L. Zhang, C. Xie, Y. Wang, Y. Guo, T. Leng, Injectable self-healing anti-inflammatory europium oxide-based dressing with high angiogenesis for improving wound healing and skin regeneration, Chemical Engineering Journal 412 (2021) 128471.
[22] M.S. Taha, G.M. Cresswell, J. Park, W. Lee, T.L. Ratliff, Y. Yeo, Sustained delivery of carfilzomib by tannic acid-based nanocapsules helps develop antitumor immunity, Nano letters 19(11) (2019) 8333-8341.
[23] Z. Li, X. Huang, L. Lin, Y. Jiao, C. Zhou, Z. Liu, Polyphenol and Cu2+ surface-modified chitin sponge synergizes with antibacterial, antioxidant and pro-vascularization activities for effective scarless regeneration of burned skin, Chemical Engineering Journal 419 (2021) 129488.
[24] Z. Wu, W. Deng, J. Luo, D. Deng, Multifunctional nano-cellulose composite films with grape seed extracts and immobilized silver nanoparticles, Carbohydrate polymers 205 (2019) 447-455.
[25] X. Ma, Y. Cheng, H. Jian, Y. Feng, Y. Chang, R. Zheng, X. Wu, L. Wang, X. Li, H. Zhang, Hollow, rough, and nitric oxide-releasing cerium oxide nanoparticles for promoting multiple stages of wound healing, Advanced healthcare materials 8(16) (2019) 1900256.
[26] A. Lipatov, H. Lu, M. Alhabeb, B. Anasori, A. Gruverman, Y. Gogotsi, A. Sinitskii, Elastic properties of 2D Ti3C2Tx MXene monolayers and bilayers, Science advances 4(6) (2018) eaat0491.
[27] H. Liang, J. Li, Y. He, W. Xu, S. Liu, Y. Li, Y. Chen, B. Li, Engineering multifunctional films based on metal-phenolic networks for rational pH-responsive delivery and cell imaging, ACS Biomaterials Science & Engineering 2(3) (2016)

317-325.
[28] A. Ricci, K.J. Olejar, G.P. Parpinello, P.A. Kilmartin, A. Versari, Application of Fourier transform infrared (FTIR) spectroscopy in the characterization of tannins, Applied Spectroscopy Reviews 50(5) (2015) 407-442.
[29] K. Wang, Y. Zhou, W. Xu, D. Huang, Z. Wang, M. Hong, Fabrication and thermal stability of two-dimensional carbide Ti3C2 nanosheets, Ceramics International 42(7) (2016) 8419-8424.
[30] Q. Xue, H. Zhang, M. Zhu, Z. Pei, H. Li, Z. Wang, Y. Huang, Y. Huang, Q. Deng, J. Zhou, Photoluminescent Ti3C2 MXene quantum dots for multicolor cellular imaging, Advanced Materials 29(15) (2017) 1604847.
[31] F. He, B. Zhu, B. Cheng, J. Yu, W. Ho, W. Macyk, 2D/2D/0D TiO2/C3N4/Ti3C2 MXene composite S-scheme photocatalyst with enhanced CO2 reduction activity, Applied Catalysis B: Environmental 272 (2020) 119006.
[32] Y. Liao, J. Qian, G. Xie, Q. Han, W. Dang, Y. Wang, L. Lv, S. Zhao, L. Luo, W. Zhang, 2D-layered Ti3C2 MXenes for promoted synthesis of NH3 on P25 photocatalysts, Applied Catalysis B: Environmental 273 (2020) 119054.
[33] K. Adstedt, M.L. Buxton, L.C. Henderson, D.J. Hayne, D. Nepal, Y. Gogotsi, V.V. Tsukruk, 2D graphene oxide and MXene nanosheets at carbon fiber surfaces, Carbon 203 (2023) 161-171.
[34] B. Anasori, Û.G. Gogotsi, 2D metal carbides and nitrides (MXenes), Springer2019.
[35] Y. Chen, L. Wang, J. Shi, Two-dimensional non-carbonaceous materials-enabled efficient photothermal cancer therapy, Nano Today 11(3) (2016) 292-308.
[36] J. Zeng, D. Goldfeld, Y. Xia, A Plasmon-Assisted optofluidic (PAOF) system for measuring the photothermal conversion efficiencies of gold nanostructures and controlling an electrical switch, Angewandte Chemie 125(15) (2013) 4263-4267.
[37] C.M. Hessel, V.P. Pattani, M. Rasch, M.G. Panthani, B. Koo, J.W. Tunnell, B.A. Korgel, Copper selenide nanocrystals for photothermal therapy, Nano letters 11(6) (2011) 2560-2566.
[38] W. Yin, L. Yan, J. Yu, G. Tian, L. Zhou, X. Zheng, X. Zhang, Y. Yong, J. Li, Z. Gu, High-throughput synthesis of single-layer MoS2 nanosheets as a near-infrared photothermal-triggered drug delivery for effective cancer therapy, ACS nano 8(7) (2014) 6922-6933.
[39] K.J. Kim, E.-S. Hwang, M.-J. Kim, J.-H. Park, D.-O. Kim, Antihypertensive effects of polyphenolic extract from Korean red pine (Pinus densiflora Sieb. et Zucc.) bark in spontaneously hypertensive rats, Antioxidants 9(4) (2020) 333.
[40] L. Lorencova, T. Bertok, E. Dosekova, A. Holazova, D. Paprckova, A. Vikartovska, V. Sasinkova, J. Filip, P. Kasak, M. Jerigova, Electrochemical performance of Ti3C2Tx MXene in aqueous media: towards ultrasensitive H2O2 sensing, Electrochimica acta 235 (2017) 471-479.
[41] J. Zheng, B. Wang, Y. Jin, B. Weng, J. Chen, Nanostructured MXene-based biomimetic enzymes for amperometric detection of superoxide anions from HepG2 cells, Microchimica Acta 186(2) (2019) 1-9.
[42] L.Q. Xu, K.-G. Neoh, E.-T. Kang, Natural polyphenols as versatile platforms for material engineering and surface functionalization, Progress in Polymer Science 87 (2018) 165-196.
[43] M. Fu, Y. Zhao, Y. Wang, Y. Li, M. Wu, Q. Liu, Z. Hou, Z. Lu, K. Wu, J. Guo, On-Demand Removable Self-Healing and pH-Responsive Europium-Releasing Adhesive Dressing Enables Inflammatory Microenvironment Modulation and Angiogenesis for Diabetic Wound Healing, Small 19(3) (2023) 2205489.
[44] K. Wu, W. Hua, X. Li, J. Lin, Facile pH-responsive injectable polyphenol-europium assembly coordination complex with enhanced antioxidation and angiogenesis for myocardial infarction treatment, Chemical Engineering Journal 446 (2022) 136835.
[45] Y. Huang, J. Jiang, J. Ren, Y. Guo, Q. Zhao, J. Zhou, Y. Li, R. Chen, A Fibrinogen-Mimicking, Activated-Platelet-Sensitive Nanocoacervate Enhances Thrombus Targeting and Penetration of Tissue Plasminogen Activator for Effective Thrombolytic Therapy, Advanced Healthcare Materials 11(19) (2022) 2201265.
[46] K. Rasool, M. Helal, A. Ali, C.E. Ren, Y. Gogotsi, K.A. Mahmoud, Antibacterial activity of Ti3C2T x MXene, ACS

nano 10(3) (2016) 3674-3684.
[47] C. Papuc, G.V. Goran, C.N. Predescu, V. Nicorescu, G. Stefan, Plant polyphenols as antioxidant and antibacterial agents for shelf - life extension of meat and meat products: Classification, structures, sources, and action mechanisms, Comprehensive Reviews in Food Science and Food Safety 16(6) (2017) 1243-1268.
[48] N. Sahiner, S. Sagbas, M. Sahiner, C. Silan, N. Aktas, M. Turk, Biocompatible and biodegradable poly (Tannic Acid) hydrogel with antimicrobial and antioxidant properties, International journal of biological macromolecules 82 (2016) 150-159.
[49] J. Guo, W. Sun, J.P. Kim, X. Lu, Q. Li, M. Lin, O. Mrowczynski, E.B. Rizk, J. Cheng, G. Qian, J. Yang, Development of tannin-inspired antimicrobial bioadhesives, Acta Biomaterialia 72 (2018) 35-44.
[50] B. Kaczmarek, Tannic acid with antiviral and antibacterial activity as a promising component of biomaterials—A minireview, Materials 13(14) (2020) 3224.
[51] Z. Ding, X. Wang, S. Liu, S. Zhou, R.A. Kore, S. Mu, X. Deng, Y. Fan, J.L. Mehta, NLRP3 inflammasome via IL-1β regulates PCSK9 secretion, Theranostics 10(16) (2020) 7100.
[52] Y.-N. Zhang, R. Zhao, J. Cao, B. Chen, D. Luo, J. Lu, M.Z. Iqbal, Q. Zhang, X. Kong, Multivalent effects of heptamannosylated β-cyclodextrins on macrophage polarization to accelerate wound healing, Colloids and Surfaces B: Biointerfaces 208 (2021) 112071.
[53] Y. Zhao, T. Zhang, X. Guo, C.K. Wong, X. Chen, Y.L. Chan, C.C. Wang, S. Laird, T.C. Li, Successful implantation is associated with a transient increase in serum pro-inflammatory cytokine profile followed by a switch to anti-inflammatory cytokine profile prior to confirmation of pregnancy, Fertility and Sterility 115(4) (2021) 1044-1053.
[54] K.-a. Johnson, N. Muzzin, S. Toufanian, R.A. Slick, M.W. Lawlor, B. Seifried, P. Moquin, D. Latulippe, T. Hoare, Drug-impregnated, pressurized gas expanded liquid-processed alginate hydrogel scaffolds for accelerated burn wound healing, Acta Biomaterialia 112 (2020) 101-111.
[55] X. Zheng, Z. Ding, W. Cheng, Q. Lu, X. Kong, X. Zhou, G. Lu, D.L. Kaplan, Microskin-Inspired Injectable MSC-Laden Hydrogels for Scarless Wound Healing with Hair Follicles, Advanced healthcare materials 9(10) (2020) 2000041.
[56] S. Korntner, C. Lehner, R. Gehwolf, A. Wagner, M. Grütz, N. Kunkel, H. Tempfer, A. Traweger, Limiting angiogenesis to modulate scar formation, Advanced Drug Delivery Reviews 146 (2019) 170-189.
[57] L. Huang, Y. Li, Y. Du, Y. Zhang, X. Wang, Y. Ding, X. Yang, F. Meng, J. Tu, L. Luo, Mild photothermal therapy potentiates anti-PD-L1 treatment for immunologically cold tumors via an all-in-one and all-in-control strategy, Nature communications 10(1) (2019) 1-15.
[58] Q. Chen, Q. Hu, E. Dukhovlinova, G. Chen, S. Ahn, C. Wang, E.A. Ogunnaike, F.S. Ligler, G. Dotti, Z. Gu, Photothermal therapy promotes tumor infiltration and antitumor activity of CAR T cells, Advanced Materials 31(23) (2019) 1900192.
[59] W.E. Paul, R.A. Seder, Lymphocyte responses and cytokines, Cell 76(2) (1994) 241-251.

Declaration of Interest Statement

- The manuscript has not been previously published, is not currently submitted for review to any other journal, and will not be submitted elsewhere before a decision is made by this journal.

- All authors have made a significant contribution to the findings and methods in the paper.

- All authors have read and approved the final draft.

- The work has not already been published and has not been submitted simultaneously to any other journal.

- This work was supported by National Key Research and Development Program of China (grant no. 2018YFC0311103), Project of Science and Technology Innovation Cultivation for University Students of Guangdong Province (grant no. pdjh202010062), Science and Technology Project of Guangzhou City (grant no. 2018020100), General Program of China Postdoctoral Science Foundation (grant no. 2021M701599), and National Natural Science Foundation of China (grant no. 32201083).